Measurement 222 (2023) 113683

Contents lists available at ScienceDirect

Measurement

journal homepage: www.elsevier.com/locate/measurement

Multisine impedimetric monitoring with an in-depth distribution of relaxation times analysis of WE43 and AZ31 magnesium alloys corrosion

Maria A. Osipenko [a,b], Jakub Karczewski [a], Michał Dominów [a], Marta Prześniak-Welenc [a], Iryna V. Makarava [a,c,d], Irina Kurilo [b], Dzmitry S. Kharytonau [e,*], Jacek Ryl [a,*]

[a] Advanced Materials Center and Institute of Nanotechnology and Materials Engineering, Gdańsk University of Technology, 80-233 Gdańsk, Poland
[b] Department of Physical, Colloid and Analytical Chemistry, Belarusian State Technological University, Minsk 220006, Belarus
[c] School of Engineering Science, Lappeenranta-Lahti University of Technology LUT, Yliopistonkatu 34, FI-53850, Finland
[d] Department of Chemical and Metallurgical Engineering (CMET), School of Chemical Engineering, Aalto University, P.O. Box 12200, FI-00076, Aalto, Finland
[e] Jerzy Haber Institute of Catalysis and Surface Chemistry, Polish Academy of Sciences, Krakow 30-239, Poland

ARTICLE INFO

Keywords:
Dynamic impedance spectroscopy
Distribution of relaxation times
Magnesium corrosion
Non-stationary process
Real-time corrosion monitoring

ABSTRACT

This research aims to develop and utilize an impedance-based tool for monitoring non-stationary electrochemical processes, coupling the multisinusoidal perturbation signal approach and distribution of relaxation times (DRT) analysis for the first time. The approach was used to distinguish independent processes occurring at the surface of AZ31 and WE43 Mg alloys undergoing corrosion in Hank's Balanced Salt Solution at 37 °C. We highlighted two common processes related to corrosion product layer formation. Detailed DEIS-DRT analysis was capable of real-time identification of a unique third process for the WE43 alloy, resulting from a spatially localized filiform corrosion attack in the vicinity of intermetallic particles. The proposed tool proved to be highly efficient in terms of studying non-stationary processes, while the DRT analysis allowed for an in-depth and precise localization of the number and the kinetics of the ongoing processes. The corrosion mechanism description was supported by numerous microscopic and spectroscopic tools.

1. Introduction

The widespread industrial use of magnesium and its alloys is associated with their attractive characteristics, such as a high strength-to-weight ratio, high thermal conductivity, excellent casting properties, possibility of secondary recycling, and use in the medical field as biodegradable metallic materials [1–3]. In medicine, using medical devices made of magnesium alloys attracts the attention of researchers not only due to the good biocompatibility and mechanical properties similar to native bone, but also due to the bioabsorbable properties, which eliminate the need for their secondary removal. To work efficiently, the time of the degradation process should correspond to the need [4–6]. However, unsatisfactory corrosion resistance due to the high electronegative potential of magnesium and an unstable natural surface oxide-hydroxide film lead to a rapid decrease in the mechanical stability of implants and the inability to efficiently control their degradation in time.

One of the main ways to solve the problem of low corrosion resistance of magnesium is to optimize its phase composition through alloying [7]. At present, there are two main groups of alloying elements of magnesium alloys [2,8]. The first group, AZ series, includes the alloying of Mg by aluminum (3–13 %), zinc (0.5–3.0 %) and manganese (0.1–0.4 %), which leads to an increase in hardness and tensile strength, with the strongest effect at an aluminum concentration up to 6 % [9], in particular in chloride-containing media [10,11]. Like aluminum, zinc causes an increase in tensile strength and corrosion resistance [12], while small amounts of manganese transform impurities by heavier metals (i.e. Fe), forming new intermetallic particles (IMPs) and suppressing their cathodic activity [13,14]. However, the amount of manganese must be strictly controlled, as this alloying element decreases the corrosion resistance [15]. Commercial AZ31 alloy is currently being actively tested for its use as biodegradable biomaterials.

The second group includes magnesium alloys alloyed by rare-earth elements (REEs), which are highly soluble in the α-Mg matrix. This can significantly improve the corrosion resistance and mechanical properties, especially ductility and strength, due to the formation of IMPs dispersed in the alloy matrix and precipitation strengthening [16–18]. Alloying with yttrium reduces the degradation of magnesium

* Corresponding authors.
E-mail addresses: dmitry.kharitonov@ikifp.edu.pl (D.S. Kharytonau), jacek.ryl@pg.edu.pl (J. Ryl).

https://doi.org/10.1016/j.measurement.2023.113683
Received 31 January 2023; Received in revised form 30 June 2023; Accepted 7 October 2023
Available online 9 October 2023

alloys due to the possible formation of a passive Y_2O_3 layer, which will inhibit cathodic reactions, but this does not eliminate microgalvanic corrosion, since yttrium-containing IMPs will act as the cathode for the magnesium matrix [19]. The Mg-Y-Nd-Zr systems, such as in commercially available WE43, are the most popular magnesium rare earth alloys, exhibiting even greater corrosion resistance with increasing exposure time, through immediately after immersion. This may indicate that the formed Mg–Me–O oxide film, where Me = Zr and Nd, is more stable than magnesium oxide/hydroxide [20]. In Hank's Balanced Salt Solution (HBSS), Y_2O_3 protective film contributed mainly to low cathode current density and high surface resistance [21]. Thus, WE43 demonstrates an excellent combination of mechanical and biological properties, which makes them a promising material for using as degradable implants [22,23].

Although the application potential of Mg alloys in biomedical devises is clear, accurate and reliable monitoring of the biodegradation rate of Mg alloys is still a challenge [2,24,25]. To access *in vivo* testing involving animals and then humans, a thorough *in vitro* biodegradation analysis must be initially performed. There are numerous reports on determining the corrosion rate for commercial Mg-alloys in engineering- (mostly NaCl and/or Na_2SO_4) and biomedical-relevant (HBSS, simulated body fluid (SBF), phosphate buffered saline (PBS), and Ringer's solution) media [2,24,26–28]. The methods used to evaluate *in vitro* corrosion resistance of Mg alloys can be basically divided into two groups: unpolarized (weight loss, hydrogen evolution, pH monitoring) and electrochemical (polarization techniques and electrochemical impedance spectroscopy (EIS)) measurements. The weight loss and hydrogen evolution methods are time-consuming and do not provide information on the kinetics of the degradation process. Potentiodynamic polarization is the most used electrochemical technique to estimate the corrosion rate of metallic materials [24]. In terms of biodegradation, polarization measurements offer significant kinetic information and quantification of the relative rates of the anodic and cathodic reactions, which is vital when attempting to understand the mechanistic aspects of the biodegradation process. However, this method is destructive and only provides instantaneous corrosion rates, which do not coincide well with a long-term study [29].

In this regard, implementing impedimetric measurements is preferable since they characterize the electrode/electrolyte interface at low overpotentials and are nondestructive. They can also be used over longer periods of biodegradation to detect individual interface layers on the surface of Mg alloys and study the formation of corrosion products or passivation layers [25,30]. However, classical EIS also has its own limitations. To obtain reliable EIS data, the examined system must fulfill the three cardinal requirements of linearity, causality, and stationarity. In the case of corrosion in biological media, the corroding surface of Mg alloys itself is very dynamic and changes in time due to its biodegradation, interaction of corrosion products with the ions presented in the media, and resulting changes in near-interface pH. Therefore, achieving the stability requirement is practically impossible. In practice, it makes low-frequency measurements difficult, and low-frequency spectral drift may occur [24]. Summarizing, only a combination of hydrogen evolution, polarization, and EIS data can provide accurate instantaneous and long-term determination of the degradation rate of Mg alloys in *in vitro* conditions.

Recently, an extension of the classical EIS, called dynamic EIS (DEIS) has been used to examine the corrosion process of Al [31–33] and Mg alloys [34]. The DEIS technique makes it possible to receive instantaneous impedance spectra by a multisinusoidal perturbation signal instead of the classical frequency-by-frequency EIS approach [35,36]. The measurement duration is determined by the lowest frequency applied, which in DEIS is typically limited to Hz range. Therefore, this approach reflects the dynamics of the investigated process and overcomes the stationarity problem. In some cases [37,38] DEIS was applied to analyze corrosion kinetics of Mg alloys in potentiodynamic conditions. In the case of *in vitro* tests, EIS measurements performed at the open-circuit potential (OCP) are of particular interest, while its value maybe be subject to change during prolonged corrosion monitoring. Thus, in this work, DEIS operated in galvanostatic mode under $i_{DC} = 0$.

Typically, EIS experimental data are analyzed by fitting to a suitable equivalent circuit. Such an equivalent circuit can be built with electrical analogues, however, in the case of the complex systems, the electrochemical processes are often overlapping, and it may be difficult or even impossible to propose an appropriate equivalent circuit. In addition, analyzing data using an equivalent circuit requires a priori assumption of the expected processes. In the case of complex electrochemical systems, in which some additional processes may occur during operation, such an assumption may lead to misunderstanding or misinterpretation of the occurring phenomena [39]. An alternative way to analyze impedance spectroscopy data is to transform it into a τ domain using distribution function of relaxation times (DRT) [40,41]. The main goal of DRT is to identify the characteristic distribution of typical EIS timescales. The relation between the impedance spectrum Z(ω) and distribution function of relaxation times γ(τ) is given by Eq. (1).

$$Z(\omega) = R_0 + R_P \int_0^{\infty} \frac{\gamma(\tau)}{1 + j\omega\tau} d\tau \quad (1)$$

where R_P represents the total polarization resistance and R_0 is its ohmic part. γ(τ) is a normalized function, where $\int_0^{\infty} \gamma(\tau) d\tau = 1$. This relation is valid for all systems that fulfill the linearity demand of impedance spectroscopy. If we consider the system as a finite set of RC elements, each peak in the γ(τ) function represents a polarization process and is characterized by a position of the peak's maximum related with the time constant of the process τ = RC and by an area enclosed under the peak corresponding to its resistance. The DRT analysis is extensively used to examine the kinetics of the electrode processes in fuel cells and batteries and to evaluate their degradation over time [42–45]. In the field of corrosion processes, the usage of DRT to analyze EIS data is very limited and only several papers exist [46].

This work proposes a new approach to integrating multisine impedimetric monitoring by DEIS with an in-depth, real-time DRT analysis as an expedient method to examine the kinetics of non-stationary corrosion process of Mg alloys in biologically relevant media. Thus, two commercial Mg alloys, WE43 and AZ31, containing different alloying elements and considered to be promising for implant materials were selected. Their long-time corrosion monitoring was combined with inductively coupled plasma-optical emission spectrometry (ICP-OES), X-ray photoelectron spectroscopy (XPS), and scanning electron spectroscopy (SEM) to propose mechanisms of their corrosion in HBSS. To the best of the authors' knowledge, this is the first ever approach to the use of combined DEIS and DRT methodologies in corrosion studies. These systems are extensively investigated and of great practical importance associated with the use of Mg alloys as biodegradable implant materials.

2. Materials and methods

2.1. Materials

As test materials, commercially available AZ31 and WE43 Mg alloys, received from Smiths High Performance (UK), were used. The nominal chemical composition of the AZ31 alloy is (wt.%): Al 3.0 %, Zn 1.0 %, Mn 0.3 %, and Mg balance. The nominal chemical composition of the WE43 Mg alloy includes (wt.%): Nb 2.2 %, Y 3.7 %, Zr 0.5 %, and Mg balance.

Samples of the alloys with sizes 20 × 20 × 3 mm^3 were cut from the as-received plate and round bar and further investigated. For electrochemical measurements, the samples were sanded in 99.9 % ethanol to P2500-grit with emery paper without further polishing. For microstructure measurements, samples were further polished up to 0.3 μm with diamond paste and non-aqueous lubricant.

Corrosion monitoring was carried out in HBSS (pH = 7.2). Its chemical composition is as follows (g/L): 8.0 NaCl, 0.4 KCl, 0.14 $CaCl_2$, 0.2 $MgSO_4 \cdot 7H_2O$, 0.1 $MgCl_2 \cdot 6H_2O$, 0.35 $Na_2HPO_4 \cdot 2H_2O$, 0.06 KH_2PO_4 and 0.35 $NaHCO_3$ [26]. All the chemicals were purchased from Merck Life Science and ChemPur and were of analytical reagent grade.

2.2. Impedimetric monitoring and data analysis

The electrochemical impedance monitoring was performed in a three-electrode setup. A saturated Ag/AgCl electrode was used as the reference electrode, a Pt mesh was used as the counter electrode, and the investigated magnesium alloys were used as the working electrode. The working area was 0.6 cm^2. The corrosion cell volume was 45 mL. A heating immersion thermostat (Julabo, Germany) was used to maintain a constant temperature of 37 °C.

The dynamic electrochemical impedance spectroscopy (DEIS) measurements were carried out in galvanostatic mode at $i_{DC} = 0$ to imitate open circuit potential (OCP) conditions. The AC perturbation signal was composed of elementary sine waves in the frequency range from 22000 Hz to 7 Hz with 10 points per decade of frequency. The sampling frequency was 128 kHz. Impedance spectra were recorded for 12 h. Further details on the experimental setup and the measurement conditions are presented elsewhere [47].

Impedance data were analyzed with the DRT method using the DRTTools software [48]. The analysis used second order regularization derivative with regularization parameter 10^{-7}. In order to cope with the large amount of raw data created by DEIS, an automated algorithmic analysis of the acquired spectra was developed. Preparation and analysis of the data was automated with a Python script using a graphical user interface automation method. The next step in the analysis was performed by calculating the positions of the peaks in separate DRT plots and creating an algorithm to search for continuous processes. For each point, the closest neighboring points in the specified range in the next plot were found. If repeating this procedure for every point revealed the occurrence of a continuous peak, it was identified as an electrochemical process. After removing the shortest processes (identified as measurement artefacts by having a time duration less than 5 % of the longest process), the charge transfer resistances and capacitances were calculated for each point.

2.3. Physico-chemical and surface analysis techniques

All physicochemical studies were conducted at pre-selected times (10 min, 1, 3, 6 and 12 h of WE43 and AZ31 alloys' exposure to HBSS as the corrosion media) to correlate with the obtained DEIS and DRT results, unless stated otherwise.

The microstructure of the WE43 and AZ31 alloys' surfaces, as polished and after exposure to HBSS, was studied using a FEI Quanta 250 FEG Scanning Electron Microscope (SEM), under an accelerating voltage of 20 kV. An Energy Dispersive X-Ray Spectroscopy (EDX) detector (Thermo Fisher Scientific) attached to the SEM was used to study the chemical composition in the same operating conditions. An Olympus LEXT OLS4000 confocal scanning laser microscope was used to examine the topography of the studied alloys' surfaces. Images were obtained using a 405 nm laser and a photomultiplier detector.

The surface topography and Volta potential distribution maps were studied with an NTEGRA Aura (NT-MDT) AFM setup in non-contact mode and using HQ:NSC18 probes (MikroMasch) with platinum coating. The Volta potential maps were done using scanning Kelvin probe microscopy (SKPFM) in frequency modulation (FM) mode using an electrically conductive probe with a gold-plated tip. The magnesium sample was grounded, and the bias potential was applied to the tip. The Volta potential maps were not inverted. Thus, higher Volta potentials indicate an anodic character, while lower Volta potentials indicate a cathodic character of the surface. The image scan size was 10×10 μm^2.

High-resolution X-ray Photoelectron Spectroscopy (XPS) studies were carried in the core-level binding energy range of C 1 s, Mg 1 s, O 1 s, Al 2p, Y 2p, Nb 2p to evaluate the surface chemistry of AZ31 and WE43 alloys after 1 and 24 hr of corrosion in HBSS as the corrosion mechanism. The measurements were carried out using an Escalab 250Xi (Thermo Fisher Scientific), with an AlKα X-ray source and spot size 650 μm. The pass energy was 20 eV. The measurements were done under low-energy electron and Ar^+ ion bombardment for charge compensation, with a final peak calibration at adventitious carbon C 1 s (284.6 eV). Spectral deconvolution was carried out using the Avantage v5.9921 dedicated software provided by the spectroscope's manufacturer.

The total change of the magnesium concentration in the HBSS solution was analyzed on a Perkin Elmer Avio 220 Max ICP-OES. A five-point calibration was prepared based on the multi-standard Perkin Elmer – Instrument Calibration Standard 2 with a 100 μg/mL Mg concentration. The specific wavelength for Mg (285.231 nm) was used to determine the magnesium in the samples. The five separate batches were prepared to investigate the magnesium concentration after the 10 min, 1, 3, 6, 12, and 24-hour corrosion processes in HBSS for WE43 and AZ31 samples. One mL of each electrolyte was diluted 10 times into 15-mL centrifuge vials containing 9 mL of 2 % HNO_3 to obtain an Mg concentration in the measurable, linear range. The total change in the magnesium concentration was determined with respect to the initial concentration of Mg in HBSS.

3. Results and discussion

3.1. Multisine impedance measurement and data analysis

Fig. 1**A and 1B** show the results of dynamic impedance spectroscopy monitoring (DEIS) of AZ31 and WE43 magnesium alloy corrosion in HBSS. At all times, the spectra are presented as a net-like semicircles, and their quality does not differ from the traditional methods of impedance measurement. Just like in typical impedance measurements, the analysis of these spectra comes to fitting the value of the assumed "a priori" equivalent circuit. In our case, we proposed the simplistic equivalent circuit $R(QR_{CT})$ used for impedance spectra fitting (graphically shown in Supplementary Information, Fig. S1**A**) since, for most of the experiment, the impedance spectra are characterized by a single capacitive loop in the measured frequency range. In the equivalent circuit, R – ohmic resistance, R_{CT} – charge transfer resistance, CPE – constant phase element, which is the sum of the capacitance of the layer of corrosion products and the capacitance of the double layer and represents the non-ideal nature and spatial heterogeneity of the layer. The CPE impedance, Z_{CPE}, is described by eq. (2).

$$Z_{CPE} = (1/Q(jw)^n) \quad (2)$$

where Q represents parallel *quasi*-capacitance, j – imaginary number, ω– angular frequency, and n is the CPE exponent. For n = 1, the CPE describes the C_{DL} of an ideal capacitor. In most corrosion systems, this parameter is in the range between 0.8 and 1 [49]. Thus, CPE exponent n is often referred to as the heterogeneity factor. In the examined system, the CPE element was attributed to the oxide film capacitance. The fitting procedure was performed using dedicated fitting software built in the LabView environment and based on the Nelder-Mead algorithm [50]. The software was successfully used in previous DEIS studies by our group [51]. An example of fitting to selected spectra of the AZ31 and WE43 magnesium alloys is shown in Fig. 1**C and 1D**.

Fig. 2**A and 2B** show the propagation of the R_{CT} values for both studied alloys with time of exposure to corrosive media. In both cases, we can observe a similar behavior, both in terms of the values and trends of the changes taking place. At the beginning of the exposure of the examined Mg alloys to the HBSS medium, the values of R_{CT} were around 200–250 Ω. The values of R_{CT} were gradually increasing with time for both alloys, reaching the values of around 2000 Ω after 12 h of corrosion in HBSS. Such behavior can be explained by the continuous formation of

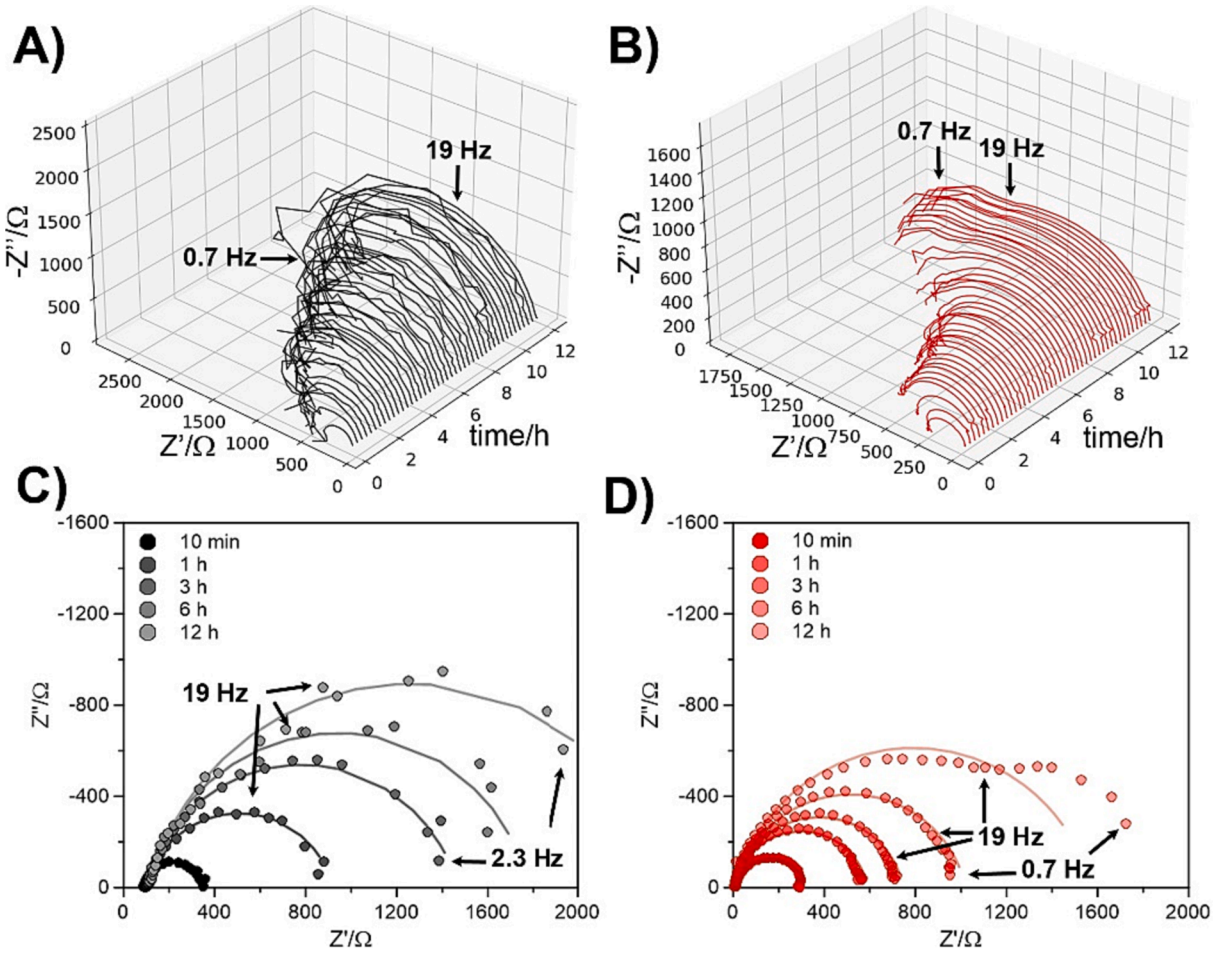

Fig. 1. DEIS monitoring of Mg alloys' corrosion in HBSS at 37 °C: A,C) AZ31, and B,D) WE43 alloy. A,B) DEIS spectra in 3D Nyquist projection vs time of exposure, C, D) classic 2D Nyquist form with imposed R(QR) EEC fitting as a solid line.

the surface film of corrosion products, which usually consists of an inner layer of MgO and a thicker, outer layer of $Mg(OH)_2$ [52,53]. At the same time, the analysis of the changes in the *quasi*-capacitance Q and CPE exponent n shown in Fig. 2**C and 2D**, revealed clearly different behavior for both alloys. For the AZ31 alloy, these parameters are almost stable and slightly decreasing with time, suggesting the presence of one electrochemical process assumed as the formation of the surface layer of corrosion products.

The situation is significantly different in the case of the WE43 alloy. Close examination of Fig. 1**D** allows us to conclude the appearance of additional processes throughout the experiment (after ca. 6 h), with 2nd capacitive loop in the Hz frequency range. At this point, the CPE exponent n decreases rapidly, eventually reaching the value of 0.7, while the proposed R(QR) EEC gradually loses its utility (See the mean square error χ^2 of the EEC fit in the **Supplementary Information file,** Fig. S2). This may suggest significant changes in processes over time and, therefore, an improperly selected equivalent circuit, as it no longer represents all the visible features. On the other hand, all the experimental data should be fitting using a single EEC for direct comparison.

The above-presented problem justifies the use of the distribution of relaxation times (DRT) analysis in our study. One of DRT's key advantages is that it does not require a priori assumptions regarding the expected results, thus allowing proper identification of the occurring processes directly from the measured data. Each peak of DRT spectra, presented in Fig. 3**A and 3B**, represents one of the electrochemical processes. The area enclosed under the peak corresponds to the process resistance and the time constant can be read from the peak positions. Theoretically, the width of the peak halves makes it possible to calculate the n parameter (the CPE exponent), however, due to the high sensitivity to the conditions of the measurement and analysis parameter, we limited ourselves to the assumption that we consider the system as a finite set of RC. The gradual shift of peak positions vs τ are highlighted in Fig. 3**C and 3D**. Selected EECs parameters obtained with the use of DRT analysis are shown in **Supplementary Information file,** Table S1.

It may be concluded that this approach allows for a more accurate analysis of the occurring phenomena, and, in particular, to provide detailed information regarding the number of electrochemical processes and their trends. Additionally, it is possible to extract the values of the polarization resistance, labeled as R_1, R_2, and R_3 for the P1, P2, and P3 process, respectively. In the case of the AZ31 alloy, initially only one dominant process (P1) was observed. After 10–15 min of the exposure of the examined Mg alloys to HBSS, the second process (P2) appears in the DRT spectra. The resistance of the P1 process (shown in Fig. 3**E**) is over 90% of the total resistance of the system, while the P2 process constituting less than 10% of the total resistance (see the plots in **Figs S3 and S4** in the **Supplementary Information file**). In the case of the WE43 alloy, the situation is similar for the first 6 h of the corrosion process, but then, in a lower frequency range, the additional electrochemical process (P3) occurs. The values of the polarization resistance R_P of two dominant processes (P1 and P3) are presented in Fig. 3**F**. After some time, they are comparable with each other. It is worth noting that the total polarization resistance for both alloys is very similar. The appearance of an additional process in the DRT range for the WE43 alloy fits perfectly with the point where the value of the n parameter of the traditional impedance spectral analysis begins to change drastically.

The analysis of the P1 and P2 processes and their evaluation in time

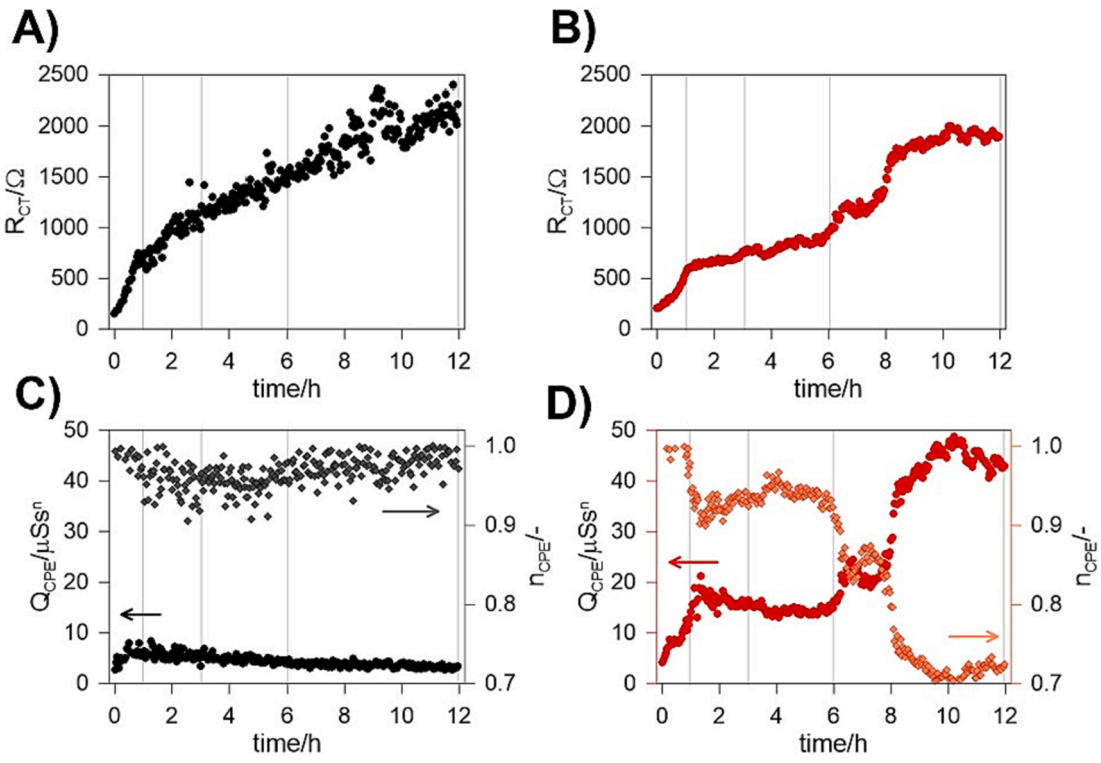

Fig. 2. DEIS monitoring of Mg alloys' corrosion in HBSS at 37 °C: A,C) AZ31, and B,D) WE43 alloy. A,B) R_{CT} deconvolution results, and C,D) CPE (Q, n) deconvolution results.

allowed to propose their roles in the corrosion mechanism of the AZ31 and WE43 alloys in HBSS. Initially, the P1 process is the only observed process in the system. Later on, it dominates in the impedance response. This parameter was assigned to the dissolution of the Mg matrix during corrosion of the examined Mg alloys. In turn, the P2 parameter was negligible in the first minutes of corrosion and later had much lower intensity. Therefore, it was linked to the progressive formation of the surface protective layer of corrosion products in the form of MgO/$Mg(OH)_2$. These assumptions do not contradict the corrosion mechanisms of Mg alloys proposed in the existing literature [2,52,54–56] and discussed below in the present contribution.

The identification of the P3 process observed in the DRT spectra of the WE43 alloy is not so straightforward. Generally, the observed differences between the DRT spectra of the studied alloys can be assigned to differences in their composition and microstructure. The P3 process can originate from either corrosion of the WE43 alloy or passivation/repassivation processes occurring on its surface. The P2 process, assigned to the deposition of the MgO layer is assumed to be the dominant passivation-related surface process in the case of the corrosion of Mg alloys. Based on this, it is possible to state that any process directly related to the surface passivation due to the REEs in the microstructure of the WE43 alloy will have the intensity comparable or lower than that of the P2 component. The comparison of the intensities between P1, P2, and P3 processes showed that the P2 process has the lowest resistance, while the intensities of P1 and P3 processes are comparable. Therefore, it is reasonable to assume that the P3 process has the same nature as the P1 component, i.e., it describes some corrosion process. The analysis of the existing literature suggests that pure Mg and its alloys containing REEs as alloying elements are prone to localized filiform or intergranular corrosion [57–59]. Therefore, the P3 process was provisionally assigned to the local filiform corrosion attack of the WE43 alloy. Additional experiments discussed below in the present contribution fully supported this assumption.

An important observation should be made, as the R_P value, estimated as the sum of the resistances of all the occurring processes ($R_P = R_1 + R_2$ or $R_1 + R_2 + R_3$) identified by the DRT study, is analogous to the R_{CT} value, calculated from DEIS by using EEC. Its comparison allows us to verify the correctness of the applied methodology. However, in the case of the DEIS analysis, the impedimetric analysis is limited to determination of the resultant of the ongoing processes, while its exact separation is impossible. The decrease in CPE exponent n for the WE43 alloy, as visible in Fig. 2**D**, hints at frequency dispersion of the capacitance due to the possible appearance of an additional corrosion process. Indeed, the appearance of this process is clearly visible in Fig. 1**D**. The DRT analysis is capable of separating (as the P3 process) and quantitatively describing it.

To conclude, the proposed analysis of the impedance spectra distinguishes various corrosion mechanisms occurring in both magnesium alloys. One can assume that both examined Mg alloys the P1 process is dominant with the P2 process of lower intensity. For the WE43 alloy, these two processes are assisted over time by the additional P3 process.

To further support the origin of all identified process and propose the corrosion mechanism of the AZ31 and WE43 alloys in HBSS, first we decided to implement the ICP-OES monitoring of the total change in the Mg^{2+} ion concentration in the electrolytic environment throughout the process. These results are summarized in Fig. 4.

The ICP-OES confirmed the combined DEIS-DRT observation regarding the corrosion susceptibility of both studied alloys. The total change in dissolved Mg species was recorded to be higher at the end of the experiment in the case of WE43 alloy, compared to AZ31, which corresponds well with the analysis of the R_{CT} changes (in DEIS) and R_P changes (in DRT) throughout the experiment. $R_{CT} \approx R_P$ for the first hours of the experiment, reflected by a similar ΔMg. On the other hand, surpassing the 3 h mark, magnesium dissolution appears to be faster for the WE43 alloy (by approx. 20 % after 12 h), again reflected by lower R_{CT}/R_P values for the WE43 alloy when compared to the AZ31 alloy. The difference in alloys corrosion resistance is more accurate when comparing the DRT results (WE43 has an approx. 20% higher R_P after 12 h) rather than DEIS (approx. 10 % higher R_{CT} after 12 h), which might be due to inaccuracy in the fitting of the DEIS EEC at higher

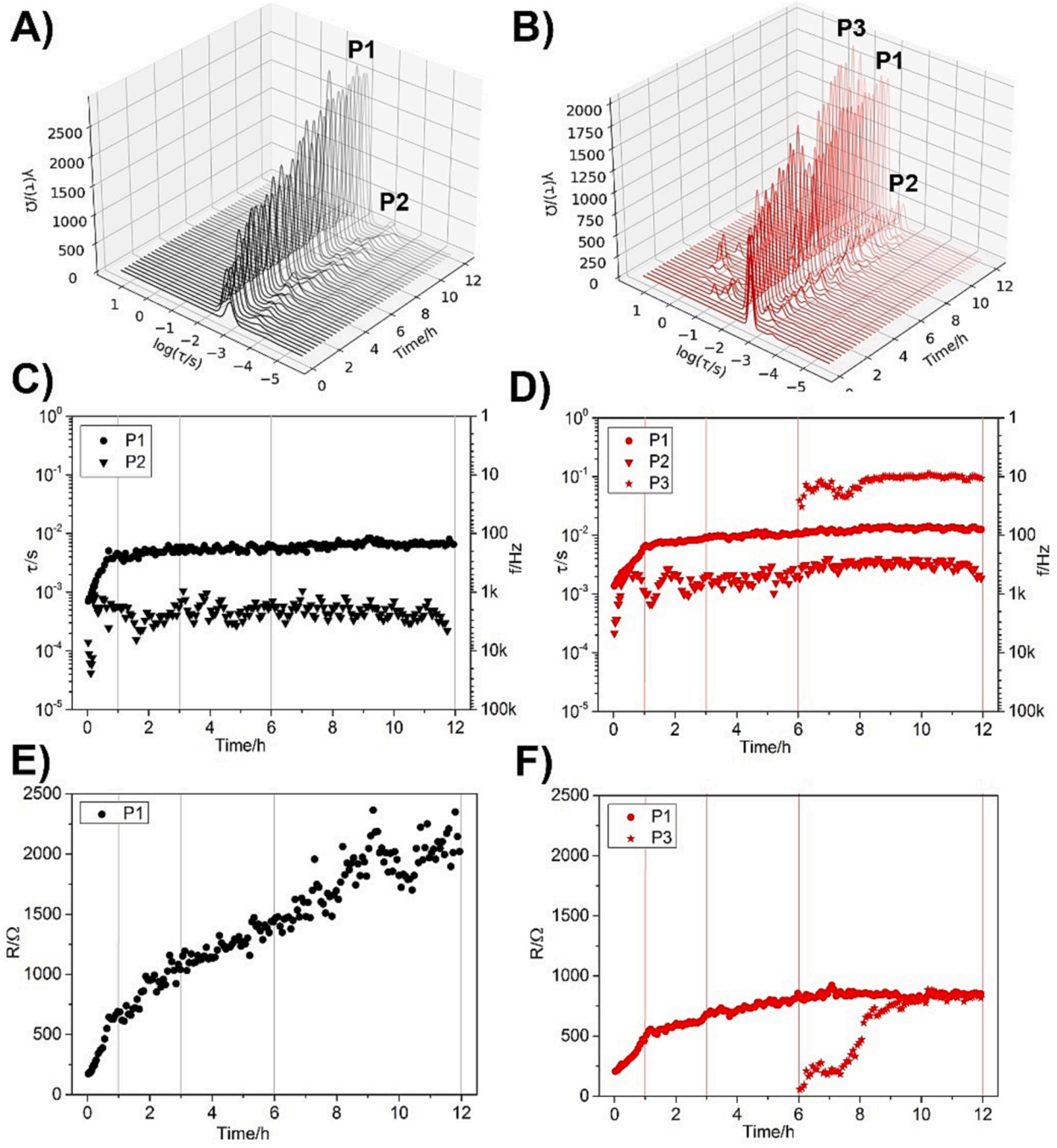

Fig. 3. DRT analysis based on DEIS analysis for A,C,E) AZ31, and B,D,F) WE43 magnesium alloys: A,B) DRT spectrograms; C,D) distribution of time constants for identified processes, and E,F) changes in the primary processes resistances (remaining resistances in the Supplementary Information file, Fig. S4).

exposure times. Such a good relationship between the electrochemical and the physicochemical Mg corrosion rate factors suggests that the primary occurrence of both P1 and P3 processes are related to the dissolution of Mg in the alloy matrix rather than alloy additives.

3.2. *Microstructure and surface chemistry changes during corrosion*

In this section, we briefly describe the microstructure of the examined AZ31 and WE43 Mg alloys. A more detailed examination of the microstructure was performed in our previous publications [60–62]. In Fig. 5**A and 5E**, the SEM micrographs reveal the microstructure of the polished AZ31 and WE43 magnesium alloys, respectively. Both alloys consist of an α-Mg-matrix and IMPs, which are significantly different in the composition and morphology depending on the alloy's nature. The AZ31 alloy is characterized by two types of IMPs: polyhedral particles with almost round and rectangular shapes detected. The maximum size of both types of IMPs does not exceed 10 μm and they are randomly distributed in the alloy matrix. The composition of IMPs based on the EDX analysis (**Supplementary Information** file, **Fig. S5** and **Table S2**) is typical for Al_xMn_y intermetallic phases and is in agreement with the literature [61,63]. Other types of AlMgZn particles with different stoichiometry are also plausible [9], but were not found in the investigated alloy. On the other hand, the IMPs present in the structure of the WE43 alloy are located primarily along the grain boundaries and characterized by a quite irregular sieve structure and size not exceeding 20 μm. According to the CALPHAD calculation for the WE43 magnesium alloy, it is

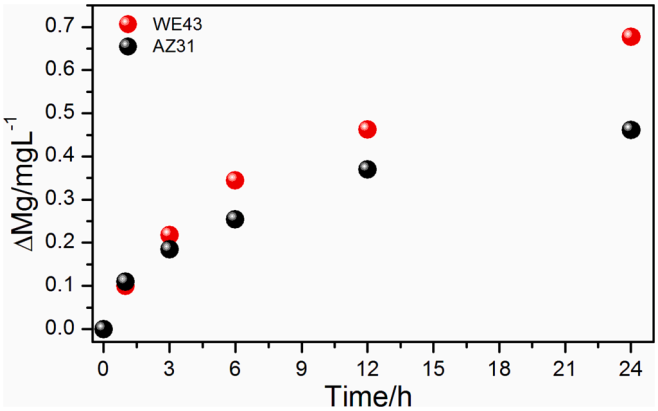

Fig. 4. ICP-OES determination of the total change in dissolved Mg concentration in the HBSS throughout the exposure for both studied Mg alloys.

possible to form particles of the $Mg_{12}RE$ and $Mg_{24}Y_5$ type, and Zr-containing particles may also occur in this alloy. Based on the point EDX analysis, these particles are made of $Mg_xNb_yY_z$-type, which corresponds to other sources [60,64].

Based on the nature of the alloying elements and the microstructure of both the studied alloys, a different electromotive force of galvanic microcells forming between the alloy matrix and the IMPs is expected. In order to predict the significance of these microcells on the corrosion behavior, we performed Scanning Kelvin Probe Force Microscopy (SKPFM) measurements, as shown in Fig. 5**B and 5F** (details in the **Supplementary Information file,** Fig. S6). The studies clearly indicate that regardless of the type of Mg alloy, in galvanic couple matrix-IMPs, the matrix will serve as the anode due to its lower Volta potential, while the IMPs will form cathodic areas. Therefore, it can be expected that the electromotive force, due to the Volta potential difference, will induce the local corrosion process at the IMP/matrix interface in electrolytic conditions. A significantly higher Volta potential difference was observed for Mg matrix-Al_xMn_y cells of AZ31 alloy (99 ± 12 mV) compared to Mg matrix-$Mg_xNb_yY_z$ of WE43 (50 ± 10 mV), which directly translates to alteration of the localized corrosion susceptibility of both alloys. The paper [65] shows that such a potential difference is typical for Al_8Mn_5 intermetallic particles.

The optical micrographs of the AZ31 and WE43 magnesium alloys after exposure to HBSS for 1 and 24 h in thermostated conditions show prominent differences in corrosion behavior. For the AZ31 alloy, the surface is covered with insoluble corrosion products, which after removal reveal a uniformly corroded surface area (Fig. 5**C and 5D**). After 24 h of corrosion monitoring, a white and yellowish, thick and compact layer of corrosion products is formed on the surface. The layer is characterized by a large number of cracks under electron microscope, which suggest its high hydration level (see **Supplementary Information file,** Fig. S7A). On the other hand, the WE43 alloy (Fig. S7B) appears to be much more vulnerable to localized corrosion, in particular microgalvanic and filiform corrosion. Fig. 5**G** shows that 1 h is sufficient to introduce localized corrosion effects located at grain and IMP boundaries (marked with red arrows). Extended exposure leads to the formation of an irregular network distribution (Fig. 5**H**). The process is initiated at the center of cathodically active sites and is claimed to be strictly correlated to the Zr concentration [57], then propagates along the aggregation zone of Cl^-. The presence of the insoluble corrosion products was restricted to the filiform corroded areas (**Supplementary Information file,** Table S3).

The surface chemistry of AZ31 and WE43 alloys after corrosion exposure were tracked with the EDX (Fig. 6**A and 6D**) and XPS techniques (Fig. 6**B, C, E and F**). The EDX analysis was focused on studying the chemical changes at the surface of the corroding Mg alloys, in particular, identification of the origin of the insoluble corrosion products layer observed under the microscope. As previously mentioned, the AZ31 alloy nearly immediately covers with a corrosion products layer, and no further changes are observed surpassing the 10 min mark. The layer might be composed of Mg oxides and/or hydroxides, made up of a significant share of Ca and P, precipitated due to the specific composition of HBSS. On the other hand, in the case of the WE43 alloy, the surface chemistry is evolving, and upon filiform corrosion attack, the amount of oxygen is significantly higher compared to AZ31 (up to 14 wt %). The analysis was averaged from ~ 1 mm^2 to include the unequal and increasing coverage by filiform corrosion.

The supporting XPS analysis was carried out after 24 h exposure to define the surface chemistry in detail, considering the large X-ray escape depth and EDX's inability to specify the chemical state of the investigated elements. These analyses were carried out in the Mg 1 s, Ca 2p, P 2p, Na 1 s, and Cl 2p core-level binding energy ranges, as well as for alloying additives Y 3d, Zr 3d (WE43) and Al 2p, Mn 2p (AZ31). The C and O were excluded from the analysis since their presence is significantly affected by air exposure during post-treatment and storage. For the WE43 alloy, separate analyses were carried out in the filiform corroded area (labeled as WE43:ff) and unaffected surface (labeled as WE).

As expected, the alloying additives have a substantial effect on the

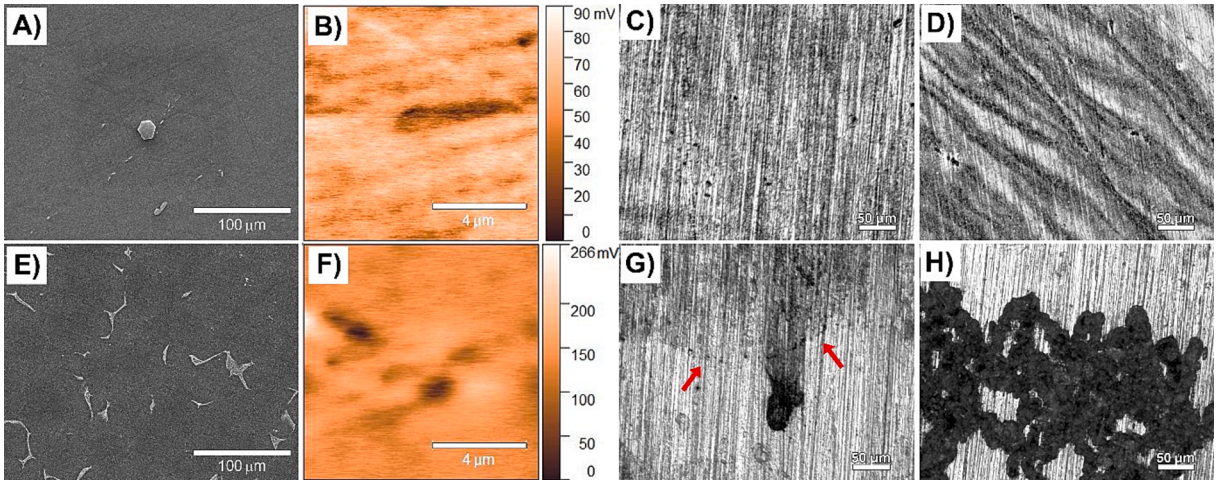

Fig. 5. Topography of the studied alloys' surface: A–D) AZ31, and E–H) WE43. A,E) SEM topography with visible IMPs after polishing; B,F) SKPFM Volta potential maps. The effect on topography of the corrosion process in HBSS after C,G) 1 h, D,H) 24 h based on confocal microscopy images. Note, the SKPFM Volta potential maps were not inverted.

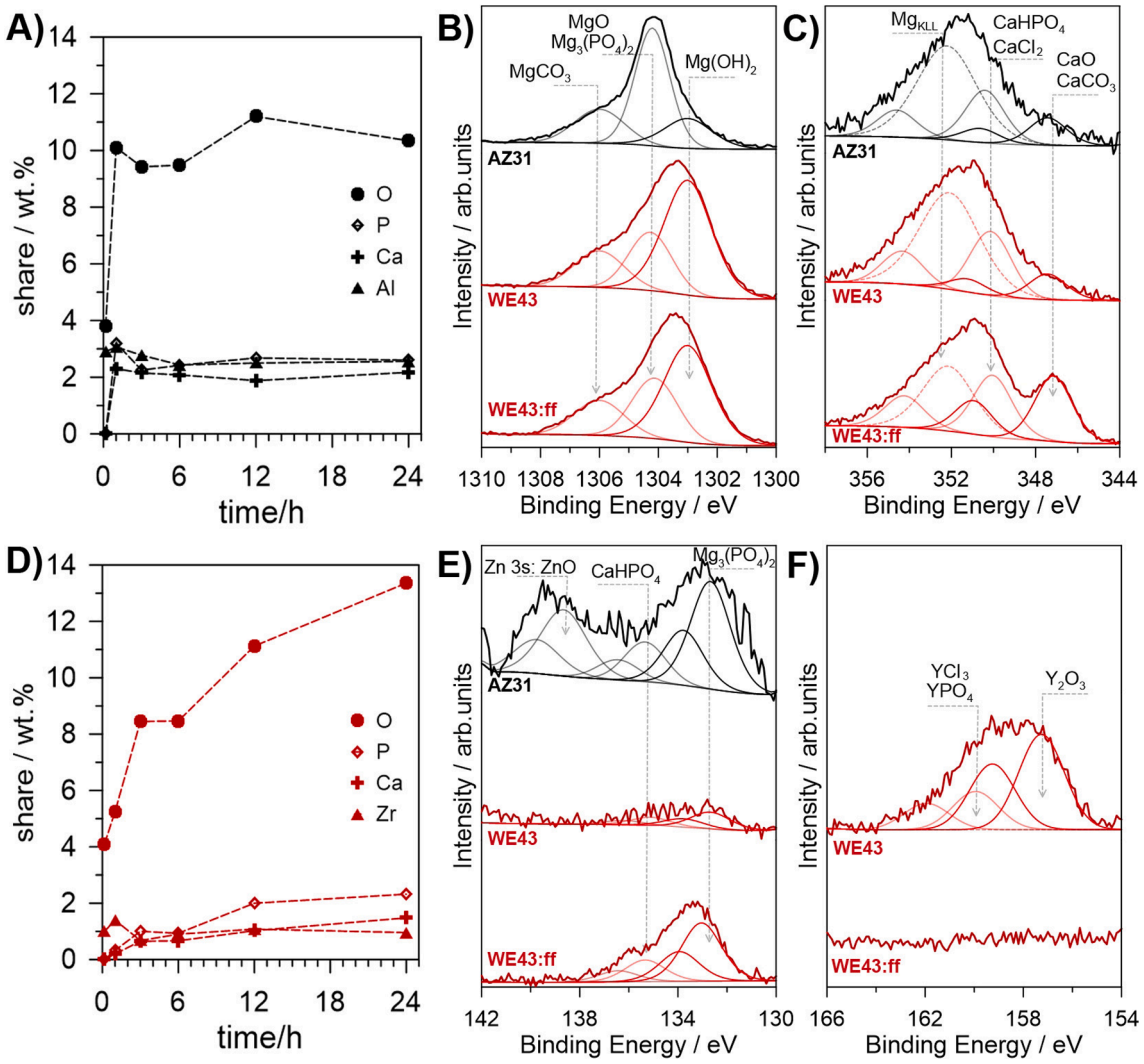

Fig. 6. A,D) EDX analysis with time of exposure of A) AZ31 and D) WE43 alloy. B,C,E,F) high-resolution XPS results with deconvolution model for AZ31 and WE43 alloys after 24 h of corrosion in HBSS: B) Mg 1 s, C) Ca 2p, E) P 2p, F) Y 3d. WE43:ff label marks the spectra recorded at filiform corroded surface.

corrosion rate and mechanism. The total share of Mg among the analyzed elements was only 45.7 at.% for AZ31, while the corrosion products layer at the AZ31 alloy surface is primarily built of MgO and/or $Mg_3(PO_4)_2$, a conclusion drawn based on the presence of an Mg 1 s peak at 1304.2 eV (57 % of total Mg) and a P 2p peak at 132.8 eV in the deconvoluted XPS spectra [66]. Apart from magnesium phosphates, the presence of $MgCO_3$ is also manifested by the peak at 1306.2 eV [67]. On the contrary, the dominant species at the surface of WE43 alloy are magnesium hydroxides $Mg(OH)_2$, while the amount of MgO / $Mg_3(PO_4)_2$ is decreased [68]. Calcium present in HBSS also precipitates at the Mg surface, most notably forming $CaHPO_4$ (Ca 2p peak at 350.1 eV) and $CaCO_3$ (at 347.2 eV) [69], however it should be emphasized that the analysis of the Ca 2p region was hindered by the overlapping of the Mg_{KLL} Auger peak at approx. 362.4 eV. Yet, the presence of $CaHPO_4$ was cross-verified by the P 2p component at 135.2 eV. Nevertheless, the calcium chemistry is quite similar between the AZ31 and WE43 alloys. These data are summarized in Table 1.

Comparison between the filiform corrosion affected (WE43:ff) and free (WE43) areas revealed no significant changes in Mg composition, and only a slightly lower $Mg(OH)_2$ share in the filiform corroded area, assisted with a higher share of adsorbed chlorides. The surface area unaffected by the filiform corrosion is nearly free of phosphates. Importantly, the presence of yttrium (up to 4.0 at.%) is only recognized in these cathodic areas, where its chemical composition suggests the presence of yttrium oxides and chlorides (or phosphates). The Zr concentration was below the spectroscope threshold level and could not be estimate, however, since the alloying additives Y, Nb and Zr form IMPs, the previously discussed Zr effect on the occurrence of filiform corrosion

Table 1
XPS quantitative analysis (in at.%) based on the proposed deconvolution model.

	Mg			**Ca**		**P**		**Y**		**Na**	**Cl**
	$Mg(OH)_2$	MgO/ $Mg_3(PO_4)_2$	$MgCO_3$	$CaCO_3$	$CaHPO_4$	$Mg_3(PO_4)_2$	$CaHPO_4$	Y_2O_3	YCl_3	inorganic	
BE/eV	1303.0	1304.2	1306.0	347.2	350.1	132.8	135.2	157.3	159.9	1071.4	199.2
AZ31	9.0	26.1	10.6	6.4	12.8	25	10.1	–	–	–	–
WE43	39.0	17.2	11.1	5.6	14.4	2.2	1.1	3.3	1.1	3.3	1.7
WE43:ff	27.0	15.8	10.1	15.4	14.9	7.7	2.9	–	–	4.8	1.4

may be indirectly associated with the local cluster-like Y distribution. Moreover, the absence of Y in the filiform affected areas may be caused by the high electronegative potential of this element and its preferential dissolution. Importantly, unlike AZ31, adsorbed chlorides were present at the surface of the WE43 alloy.

3.3. Corrosion mechanism of AZ31 and WE43 alloys in HBSS

This section summarizes the results of the present contribution and attempts to provide a more detailed corrosion mechanism of the AZ31 and WE43 magnesium alloys in HBSS. The schematic illustration of the proposed corrosion mechanism of the AZ31 and WE43 alloys in HBSS is shown in Fig. 7. These mechanisms have been developed based on the experimental data discussed in the present contribution and the available literature [13,25,56,57,60,61,70,71].

In general, biodegradation of the AZ31 and WE43 Mg alloys in HBSS solution proceeds following similar schemes with some prominent differences at later stages. Our results show that a combination of local corrosion events occurs due to galvanic coupling between IMPs and the alloy matrix and interactions of the alloy surface with the corrosion medium. This is typical for Mg alloys due to their high reactivity in aqueous media [2]. The surface of the as-polished AZ31 and WE43 alloys (Fig. 7 Ia and Ib) contains an α-Mg matrix with several types of IMPs, which is typical for these alloys [60,72,73]. The results of the EDX analysis do not support the presence of the large fraction of Zr-rich IMPs in the composition of the examined WE43 alloy, however, the DRT data and observed corrosion morphology suggest the importance of these precipitates in the corrosion events. In the first stage (Fig. 7 **IIa and IIb**), corrosion of the Mg matrixes of both examined alloys readily occurs. The mechanism of this process can be expressed by the following reactions:

$$Mg \rightarrow Mg^{2+} + 2e^{-} \quad (3)$$

$$2H_2O + 2e^{-} \rightarrow H_2 + 2OH^{-} \quad (4)$$

Corrosion attack initiates over the whole surface of the alloy and consists of the general corrosion of the Mg matrix and local corrosion over the matrix-IMP interface due to galvanic coupling [74]. The intensity of the galvanic coupling depends on the activity of each microconstituent as a cathode. In the case of the WE43 alloy, the cathodic IMPs are larger in size and surface fraction, suggesting higher local corrosion attack. The impedance response of the process (3) is a slightly distorted semicircle (Fig. 1) registered in the first minutes of corrosion monitoring. In the DRT analysis, this process in clearly seen in the spectra obtained in the first minutes of the experiment and was assigned to the P1 process (Fig. 7 **IIc**). The cathodic reaction of hydrogen evolution (Eq. (4)) occurs preferentially on IMPs, serving as local cathodes. As processes (3) and (4) propagate, the release of Mg^{2+} into the corrosion medium leads to their interaction with OH^{-} ions (Eq. (5), chemical in nature) and precipitation of a passive layer consisting mainly of Mg $(OH)_2$ on the surface (Fig. 7 **IIIa and IIIb**):

$$Mg^{2+} + 2OH^{-} \rightarrow Mg(OH)_2 \quad (5)$$

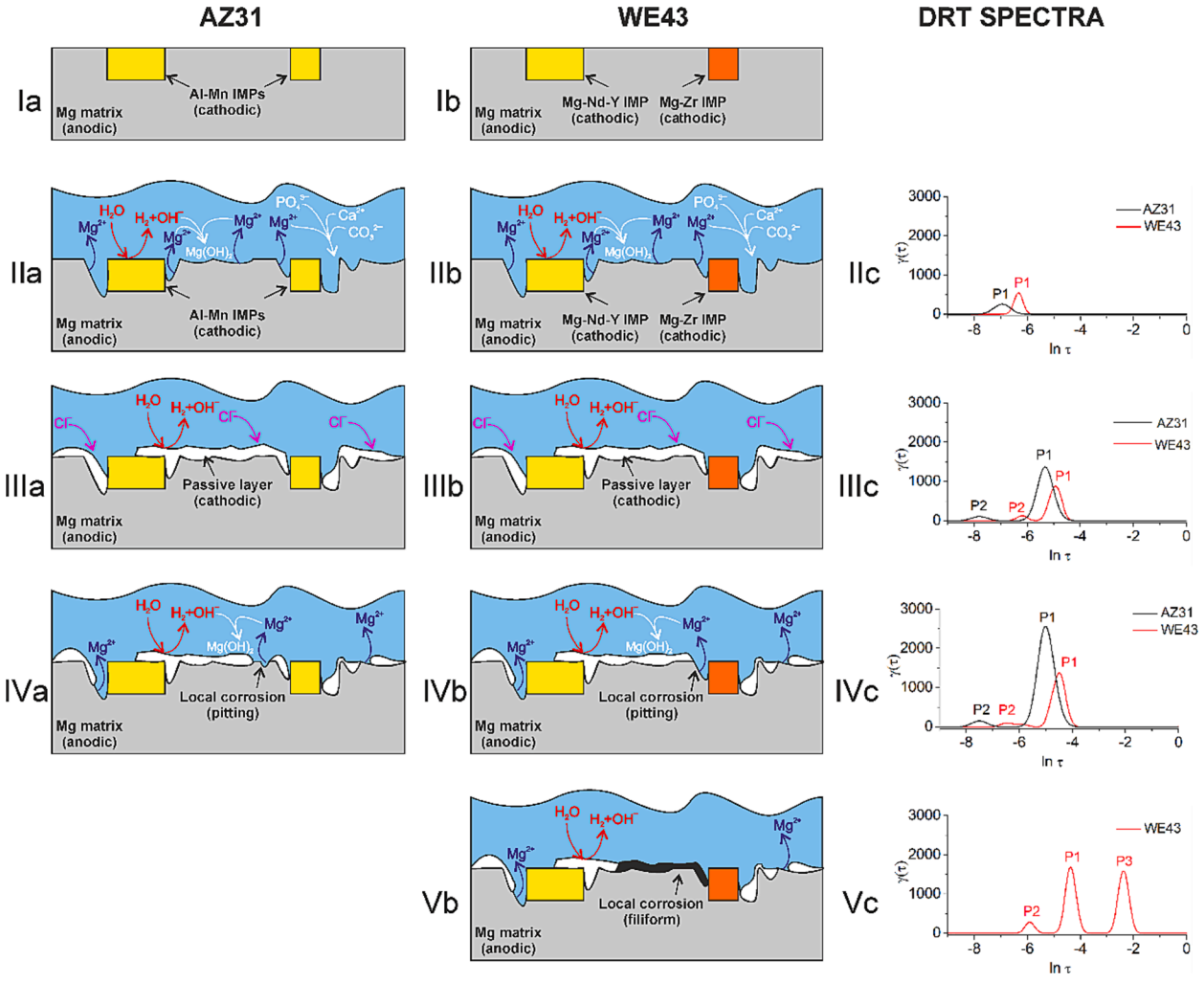

Fig. 7. Schematic illustration of stages of the AZ31 (left) and WE43 alloy (middle) corrosion in HBSS, and their corresponding DRT response (right).

The overall corrosion process in this case can be summarized as follows:

$$Mg + 2H_2O \rightarrow Mg(OH)_2 + H_2 \quad (6)$$

The released Mg^{2+} ions can interact with the components of the HBSS, leading to the precipitation of magnesium phosphates and carbonates, as suggested by the XPS analysis (Fig. 6). In turn, Ca^{2+} ions interact with hydroxides released by Eq. (4) or anions of the HBSS. They do not directly affect the corrosion processes of magnesium alloys [75] but form insoluble amorphous salts and effectively hinder the corrosion rate. Gradual thickening of corrosion products later results in the increased protective ability, as evidenced by an increase in the R_{CT} values extracted from the DEIS data. As this process is chemical in nature, the deposition of the protective film may also partially occur over cathodic IMPs, suppressing their activity [76,77]. The formation of the surface protective layer is also visible in the DRT analysis data through the occurrence of the dominant P2 process (Fig. 7 **IIIc**), whose resistance increases with time.

At this point, the relative corrosion rate of the AZ31 and WE43 Mg alloys decreases, and equilibrium between the deposition and dissolution rates of the passive layer is achieved. However, the presence of Cl^- ions results in the conversion of insoluble $Mg(OH)_2$ into soluble magnesium chloride and the development of a severe local pitting attack (Fig. 7 **IVa and IVb**) [17,56]:

$$Mg(OH)_2 + 2Cl^- \rightarrow Mg^{2+} + 2OH^- + 2Cl^- \quad (7)$$

The occurrence of deep pits on the surface of the AZ31 and WE43 alloys is clearly seen in the confocal images (Fig. 5). The onset of the localized corrosion is also visible from the results of the DEIS measurements (Fig. 1) as local drops and fluctuations in the values of R_{CT}.

In the case of the WE43 alloy, the corrosion process had one more step. For this alloy, the local corrosion attack is not suppressed in the pitting stage but proceeds further with the occurrence of surface regions of filiform corrosion (Fig. 5, Fig. 7 **Vb**). The occurrence of the filiform corrosion can be associated with the shape and surface distribution of cathodic IMPs [57,70]. As the breakdown of the initially formed surface layer of corrosion products occurs (Fig. 7 **IVb**), additional chloride ions are electrostatically attracted in pit locations, as observed in XPS analysis. The layer of filiform corrosion products over such regions appears as dark, dense surface precipitates of MgO and $Mg(OH)_2$ [54]. In the DEIS, filiform corrosion appears as the frequency dispersion of capacitance due to its localized nature, while the DRT analysis showed the occurrence of the third process, P3 (Fig. 7 **Vc**).

4. Conclusions

Within this contribution, we have delivered a new analytical approach, based on dynamic electrochemical impedance spectroscopy (DEIS) measurement coupled with a distribution of relaxation times (DRT) analysis for in-depth, real-time monitoring of the electrochemical process. We studied the non-stationary corrosion process of commercially available AZ31 and WE43 Mg alloys in environmental conditions in a biologically relevant electrolyte (HBSS).

We demonstrated that DEIS on-line monitoring is a viable and highly efficient way to track electric changes occurring at the actively corroding metal surface regardless of its non-stable nature. However, requiring selection and fitting with electric equivalent circuits, the approach is flawed when the studied conditions change. When a new process appears, it can only be tracked by changes in the distribution of relaxation times. However, the DRT analysis proposed by us allows for an effective differentiation of the number and the relaxation times of the occurring processes. In this regard, we have identified and explained each independent process.

For the first three hours of the experiment, both the AZ31 and WE43 alloys were characterized by two processes, due to Mg dissolution and the formation of insoluble corrosion products, as confirmed by EDX and ICP-OES analyses. Exceeding the above exposure time, a unique third process appears in the case of the WE43 alloy, and originates from filiform corrosion, a localized corrosion attack. The evolution of the corrosion attack mechanism was recognized by both EDX and ICP-OES, while XPS shows localization of the attack in the vicinity of Y,Zr,Nb-rich IMPs as well as the importance of the adsorption of chlorides. The susceptibility to local corrosion correlates with the activity of the galvanic microcells, formed between the alloy matrix and cathodic IMPs, as revealed by the SKPFM studies.

CRediT authorship contribution statement

Maria A. Osipenko: Data curation, Formal analysis, Investigation, Validation, Writing – original draft. **Jakub Karczewski:** Formal analysis, Methodology, Supervision, Writing – original draft, Writing – review & editing. **Michał Dominów:** Data curation, Formal analysis, Software, Validation, Visualization, Writing – original draft. **Marta Prześniak-Welenc:** Investigation, Writing – original draft. **Iryna V. Makarava:** Investigation, Validation. **Irina Kurilo:** Supervision, Writing – review & editing. **Dzmitry S. Kharytonau:** Funding acquisition, Methodology, Resources, Supervision, Writing – original draft, Writing – review & editing. **Jacek Ryl:** Conceptualization, Formal analysis, Funding acquisition, Investigation, Methodology, Project administration, Resources, Supervision, Visualization, Writing – original draft, Writing – review & editing.

Declaration of Competing Interest

The authors declare that they have no known competing financial interests or personal relationships that could have appeared to influence the work reported in this paper.

Data availability

Data will be made available on request.

Acknowledgments

Funding: This work was supported by Gdańsk University of Technology under the Aurum Supporting International Research Team Building – 'Excellence Initiative – Research University' [grant number: 2/2021/IDUB/II.1.3]. Dzmitry Kharytonau acknowledges the support by National Science Centre of Poland under Sonatina 5 [grant number: 2021/40/C/ST5/00266].

Appendix A. Supplementary data

Supplementary data to this article can be found online at https://doi.org/10.1016/j.measurement.2023.113683.

References

[1] V. Tsakiris, C. Tardei, F.M. Clicinschi, Biodegradable Mg alloys for orthopedic implants – A review, J. Magnes. Alloys. 9 (2021) 1884–1905, https://doi.org/10.1016/j.jma.2021.06.024.
[2] M. Esmaily, J.E. Svensson, S. Fajardo, N. Birbilis, G.S. Frankel, S. Virtanen, R. Arrabal, S. Thomas, L.G. Johansson, Fundamentals and advances in magnesium alloy corrosion, Prog. Mater Sci. 89 (2017) 92–193, https://doi.org/10.1016/j.pmatsci.2017.04.011.
[3] F. Witte, The history of biodegradable magnesium implants: A review☆, Acta Biomater. 6 (2010) 1680–1692, https://doi.org/10.1016/j.actbio.2010.02.028.
[4] E. Zhang, L. Xu, G. Yu, F. Pan, K. Yang, In vivo evaluation of biodegradable magnesium alloy bone implant in the first 6 months implantation, J. Biomed. Mater. Res. A 90A (2009) 882–893, https://doi.org/10.1002/jbm.a.32132.
[5] L. Yang, E. Zhang, Biocorrosion behavior of magnesium alloy in different simulated fluids for biomedical application, Mater. Sci. Eng. C 29 (2009) 1691–1696, https://doi.org/10.1016/j.msec.2009.01.014.

[6] A.H.M. Sanchez, B.J.C. Luthringer, F. Feyerabend, R. Willumeit, Mg and Mg alloys: How comparable are in vitro and in vivo corrosion rates? A Review, Acta Biomater. 13 (2015) 16–31, https://doi.org/10.1016/j.actbio.2014.11.048.

[7] M.K. Kulekci, Magnesium and its alloys applications in automotive industry, Int. J. Adv. Manuf. Technol. 39 (2008) 851–865, https://doi.org/10.1007/s00170-007-1279-2.

[8] K. Wei Guo, A review of magnesium/magnesium alloys corrosion, recent pat, Corros. Sci. 1 (2011) 72–90, https://doi.org/10.2174/2210683911101010072.

[9] N.P. Papenberg, S. Gneiger, I. Weißensteiner, P.J. Uggowitzer, S. Pogatscher, Mg-alloys for forging applications—A review, Materials. 13 (2020) 985, https://doi.org/10.3390/ma13040985.

[10] I.B. Singh, M. Singh, S. Das, A comparative corrosion behavior of Mg, AZ31 and AZ91 alloys in 3.5% NaCl solution, J. Magnes. Alloys. 3 (2015) 142–148, https://doi.org/10.1016/j.jma.2015.02.004.

[11] L. Wang, T. Shinohara, B.-P. Zhang, Corrosion behavior of Mg, AZ31, and AZ91 alloys in dilute NaCl solutions, J. Solid State Electrochem. 14 (2010) 1897–1907, https://doi.org/10.1007/s10008-010-1020-1.

[12] Y. Ding, C. Wen, P. Hodgson, Y. Li, Effects of alloying elements on the corrosion behavior and biocompatibility of biodegradable magnesium alloys: A review, J. Mater. Chem. B 2 (2014) 1912–1933, https://doi.org/10.1039/C3TB21746A.

[13] D. Höche, C. Blawert, S.V. Lamaka, N. Scharnagl, C. Mendis, M.L. Zheludkevich, The effect of iron re-deposition on the corrosion of impurity-containing magnesium, PCCP 18 (2016) 1279–1291, https://doi.org/10.1039/C5CP05577F.

[14] S.V. Lamaka, D. Höche, R.P. Petrauskas, C. Blawert, M.L. Zheludkevich, A new concept for corrosion inhibition of magnesium: Suppression of iron re-deposition, Electrochem. Commun. 62 (2016) 5–8, https://doi.org/10.1016/j.elecom.2015.10.023.

[15] N.D. Nam, M. Mathesh, M. Forsyth, D.S. Jo, Effect of manganese additions on the corrosion behavior of an extruded Mg–5Al based alloy, J. Alloy. Compd. 542 (2012) 199–206, https://doi.org/10.1016/j.jallcom.2012.07.083.

[16] L. Kong, Two main and a new type rare earth elements in Mg alloys: A review, IOP Conf. Ser. Mater. Sci. Eng. 242 (2017) 012026, https://doi.org/10.1088/1757-899X/242/1/012026.

[17] F. Witte, N. Hort, C. Vogt, S. Cohen, K.U. Kainer, R. Willumeit, F. Feyerabend, Degradable biomaterials based on magnesium corrosion, Curr. Opin. Solid State Mater. Sci. 12 (2008) 63–72, https://doi.org/10.1016/j.cossms.2009.04.001.

[18] L. Xu, X. Liu, K. Sun, R. Fu, G. Wang, Corrosion behavior in magnesium-based alloys for biomedical applications, Materials. 15 (2022) 2613, https://doi.org/10.3390/ma15072613.

[19] I. Johnson, D. Perchy, H. Liu, In vitro evaluation of the surface effects on magnesium-yttrium alloy degradation and mesenchymal stem cell adhesion, J. Biomed. Mater. Res. A 100A (2012) 477–485, https://doi.org/10.1002/jbm.a.33290.

[20] G. Ben-Hamu, D. Eliezer, K.S. Shin, S. Cohen, The relation between microstructure and corrosion behavior of Mg–Y–RE–Zr alloys, J. Alloy. Compd. 431 (2007) 269–276, https://doi.org/10.1016/j.jallcom.2006.05.075.

[21] W. He, E. Zhang, K. Yang, Effect of Y on the bio-corrosion behavior of extruded Mg–Zn–Mn alloy in Hank's solution, Mater. Sci. Eng. C 30 (2010) 167–174, https://doi.org/10.1016/j.msec.2009.09.014.

[22] S. Dobatkin, N. Martynenko, N. Anisimova, M. Kiselevskiy, D. Prosvirnin, V. Terentiev, N. Yurchenko, G. Salishchev, Y. Estrin, Mechanical properties, biodegradation, and biocompatibility of ultrafine grained magnesium alloy WE43, Materials. 12 (2019) 3627, https://doi.org/10.3390/ma12213627.

[23] E. Galvin, S. Jaiswal, C. Lally, B. MacDonald, B. Duffy, In vitro corrosion and biological assessment of bioabsorbable WE43 Mg alloy specimens, J. Manuf. Mater. Process. 1 (2017) 8, https://doi.org/10.3390/jmmp1010008.

[24] N.T. Kirkland, N. Birbilis, M.P. Staiger, Assessing the corrosion of biodegradable magnesium implants: A critical review of current methodologies and their limitations, Acta Biomater. 8 (2012) 925–936, https://doi.org/10.1016/j.actbio.2011.11.014.

[25] A.D. King, N. Birbilis, J.R. Scully, Accurate electrochemical measurement of magnesium corrosion rates; A combined impedance, mass-loss and hydrogen collection study, Electrochim. Acta 121 (2014) 394–406, https://doi.org/10.1016/j.electacta.2013.12.124.

[26] Z. Zhen, T. Xi, Y. Zheng, A review on in vitro corrosion performance test of biodegradable metallic materials, Trans. Nonferrous Met. Soc. China 23 (2013) 2283–2293, https://doi.org/10.1016/S1003-6326(13)62730-2.

[27] S. Saha, W. Lestari, C. Dini, M.N. Sarian, H. Hermawan, V.A.R. Barão, C. Sukotjo, C. Takoudis, Corrosion in Mg-alloy biomedical implants- the strategies to reduce the impact of the corrosion inflammatory reaction and microbial activity, J. Magnes. Alloys. 10 (2022) 3306–3326, https://doi.org/10.1016/j.jma.2022.10.025.

[28] G. Uppal, A. Thakur, A. Chauhan, S. Bala, Magnesium based implants for functional bone tissue regeneration – A review, J. Magnes. Alloys. 10 (2022) 356–386, https://doi.org/10.1016/j.jma.2021.08.017.

[29] Z. Qiao, Z. Shi, N. Hort, N.I. Zainal Abidin, A. Atrens, Corrosion behaviour of a nominally high purity Mg ingot produced by permanent mould direct chill casting, Corros. Sci. 61 (2012) 185–207, https://doi.org/10.1016/j.corsci.2012.04.030.

[30] Ł. Florczak, G. Nawrat, K. Darowicki, J. Ryl, J. Sieniawski, M. Wierzbińska, K. Raga, A. Sobkowiak, The effect of sodium tetrafluoroborate on the properties of conversion coatings formed on the AZ91D magnesium alloy by plasma electrolytic oxidation, Processes. 10 (2022) 2089, https://doi.org/10.3390/pr10102089.

[31] J. Wysocka, S. Krakowiak, J. Ryl, Evaluation of citric acid corrosion inhibition efficiency and passivation kinetics for aluminium alloys in alkaline media by means of dynamic impedance monitoring, Electrochim. Acta 258 (2017) 1463–1475, https://doi.org/10.1016/j.electacta.2017.12.017.

[32] J. Ryl, J. Wysocka, M. Cieslik, H. Gerengi, T. Ossowski, S. Krakowiak, P. Niedzialkowski, Understanding the origin of high corrosion inhibition efficiency of bee products towards aluminium alloys in alkaline environments, Electrochim. Acta 304 (2019) 263–274, https://doi.org/10.1016/j.electacta.2019.03.012.

[33] H. Gerengi, M.M. Solomon, E. Kaya, F.E. Bagci, E.J. Abai, An evaluation of the anticorrosion effect of ethylene glycol for AA7075-T6 alloy in 3.5% NaCl solution, Measurement 116 (2018) 264–272, https://doi.org/10.1016/j.measurement.2017.11.030.

[34] H. Gerengi, M. Cabrini, M.M. Solomon, E. Kaya, Understanding the corrosion behavior of the AZ91D alloy in simulated body fluid through the use of dynamic EIS, ACS Omega 7 (2022) 11929–11938, https://doi.org/10.1021/acsomega.2c00066.

[35] J. Ryl, R. Bogdanowicz, P. Slepski, M. Sobaszek, K. Darowicki, Dynamic electrochemical impedance spectroscopy (DEIS) as a tool for analyzing surface oxidation processes on boron-doped diamond electrodes, J. Electrochem. Soc. 161 (2014) H359–H364, https://doi.org/10.1149/2.016406jes.

[36] H. Gerengi, K. Darowicki, G. Bereket, P. Slepski, Evaluation of corrosion inhibition of brass-118 in artificial seawater by benzotriazole using Dynamic EIS, Corros. Sci. 51 (2009) 2573–2579, https://doi.org/10.1016/j.corsci.2009.06.040.

[37] A. Srinivasan, K.S. Shin, N. Rajendran, Dynamic electrochemical impedance spectroscopy (DEIS) studies of AZ31 magnesium alloy in simulated body fluid solution, RSC Adv. 4 (2014) 27791–27795, https://doi.org/10.1039/C4RA02432J.

[38] J. Orlikowski, K. Darowicki, Investigations of pitting corrosion of magnesium by means of DEIS and acoustic emission, Electrochim. Acta 56 (2011) 7880–7884, https://doi.org/10.1016/j.electacta.2010.12.021.

[39] J. Huang, N. Sullivan, A. Zakutayev, R. O'Hayre, How reliable is distribution of relaxation times (DRT) analysis? A dual regression-classification perspective on DRT estimation, interpretation, and accuracy, Electrochim. Acta (2023) 141879.

[40] D. Zhu, T. Ma, Y. Yang, Optimization and application of the distribution of relaxation times based on characteristic frequency resolution and hyperparameters, J. Power Sources 545 (2022) 231955, https://doi.org/10.1016/j.jpowsour.2022.231955.

[41] E. Quattrocchi, B. Py, A. Maradesa, Q. Meyer, C. Zhao, F. Ciucci, Deconvolution of electrochemical impedance spectroscopy data using the deep-neural-network-enhanced distribution of relaxation times, Electrochim. Acta 439 (2023) 141499, https://doi.org/10.1016/j.electacta.2022.141499.

[42] J. Kwon, P. Choi, S. Jo, H. Oh, K.-Y. Cho, Y.-K. Lee, S. Kim, K. Eom, Identification of electrode degradation by carbon corrosion in polymer electrolyte membrane fuel cells using the distribution of relaxation time analysis, Electrochim. Acta 414 (2022) 140219, https://doi.org/10.1016/j.electacta.2022.140219.

[43] Q. Zhang, D. Wang, E. Schaltz, D.-I. Stroe, A. Gismero, B. Yang, Degradation mechanism analysis and State-of-Health estimation for lithium-ion batteries based on distribution of relaxation times, J. Energy Storage. 55 (2022) 105386, https://doi.org/10.1016/j.est.2022.105386.

[44] Y. Li, Y. Jiang, J. Dang, X. Deng, B. Liu, J. Ma, F. Yang, M. Ouyang, X. Shen, Application of distribution of relaxation times method in polymer electrolyte membrane water electrolyzer, Chem. Eng. J. 451 (2023) 138327, https://doi.org/10.1016/j.cej.2022.138327.

[45] P. Córdoba-Torres, A general theory for the impedance response of dielectric films with a distribution of relaxation times, Electrochim. Acta 282 (2018) 892–904, https://doi.org/10.1016/j.electacta.2018.06.048.

[46] S. Cartagena, J.A. Calderón, Corrosion of non-noble metal-based catalysts during oxygen evolution reaction under on/off operation, Corros. Sci. 205 (2022) 110437, https://doi.org/10.1016/j.corsci.2022.110437.

[47] W. Lipińska, J. Ryl, P. Slepski, K. Siuzdak, K. Grochowska, Exploring multi-step glucose oxidation kinetics at GOx-functionalized nanotextured gold surfaces with differential impedimetric technique, Measurement 174 (2021) 109015, https://doi.org/10.1016/j.measurement.2021.109015.

[48] T.H. Wan, M. Saccoccio, C. Chen, F. Ciucci, Influence of the discretization methods on the distribution of relaxation times deconvolution: Implementing radial basis functions with DRTtools, Electrochim. Acta 184 (2015) 483–499, https://doi.org/10.1016/j.electacta.2015.09.097.

[49] C. Singh, S.K. Tiwari, R. Singh, Exploring environment friendly nickel electrodeposition on AZ91 magnesium alloy: Effect of prior surface treatments and temperature of the bath on corrosion behaviour, Corros. Sci. 151 (2019) 1–19, https://doi.org/10.1016/j.corsci.2019.02.004.

[50] F. Gao, L. Han, Implementing the nelder-mead simplex algorithm with adaptive parameters, Comput. Optim. Appl. 51 (2012) 259–277, https://doi.org/10.1007/s10589-010-9329-3.

[51] P. Niedzialkowski, P. Slepski, J. Wysocka, J. Chamier-Cieminska, L. Burczyk, M. Sobaszek, A. Wcislo, T. Ossowski, R. Bogdanowicz, J. Ryl, Multisine impedimetric probing of biocatalytic reactions for label-free detection of DEFB1 gene: How to verify that your dog is not human? Sens. Actuators B Chem. 323 (2020) 128664, https://doi.org/10.1016/j.snb.2020.128664.

[52] A. Soltan, M.S. Dargusch, Z. Shi, D. Gerrard, S. Al Shabibi, Y. Kuo, A. Atrens, Corrosion of Mg alloys EV31A, WE43B, and ZE41A in chloride- and sulfate-containing solutions saturated with magnesium hydroxide, Mater. Corros. 71 (2020) 956–979, https://doi.org/10.1002/maco.201911375.

[53] G.L. Song, A. Atrens, Corrosion mechanisms of magnesium alloys, Adv. Eng. Mater. 1 (1999) 11–33, https://doi.org/10.1002/(SICI)1527-2648(199909)1:1<11::AID-ADEM11>3.0.CO;2-N.

[54] S. Thomas, N.V. Medhekar, G.S. Frankel, N. Birbilis, Corrosion mechanism and hydrogen evolution on Mg, Curr. Opin. Solid State Mater. Sci. 19 (2015) 85–94, https://doi.org/10.1016/j.cossms.2014.09.005.

[55] S. Feliu, Electrochemical impedance spectroscopy for the measurement of the corrosion rate of magnesium alloys: Brief review and challenges, Metals. 10 (2020) 775, https://doi.org/10.3390/met10060775.
[56] M. Ascencio, M. Pekguleryuz, S. Omanovic, An investigation of the corrosion mechanisms of WE43 Mg alloy in a modified simulated body fluid solution: The influence of immersion time, Corros. Sci. 87 (2014) 489–503, https://doi.org/10.1016/j.corsci.2014.07.015.
[57] Z. Chen, H. Li, X. Liang, M.-C. Zhao, K. Zhang, A. Atrens, In-situ observation on filiform corrosion propagation and its dependence on Zr distribution in Mg alloy WE43, S2213956722002456, J. Magnes. Alloys. (2022), https://doi.org/10.1016/j.jma.2022.09.033.
[58] C. Kousis, P. Keil, H. McMurray Neil, G. Williams, The kinetics and mechanism of filiform corrosion affecting organic coated Mg alloy surfaces, Corros. Sci. 206 (2022) 110477, https://doi.org/10.1016/j.corsci.2022.110477.
[59] G. Williams, N. Birbilis, H.N. McMurray, Controlling factors in localised corrosion morphologies observed for magnesium immersed in chloride containing electrolyte, Faraday Discuss. 180 (2015) 313–330, https://doi.org/10.1039/C4FD00268G.
[60] D.S. Kharitonov, M. Zimowska, J. Ryl, A. Zieliński, M.A. Osipenko, J. Adamiec, A. Wrzesińska, P.M. Claesson, I.I. Kurilo, Aqueous molybdate provides effective corrosion inhibition of WE43 magnesium alloy in sodium chloride solutions, Corros. Sci. 190 (2021) 109664, https://doi.org/10.1016/j.corsci.2021.109664.
[61] M.A. Osipenko, D.S. Kharytonau, A.A. Kasach, J. Ryl, J. Adamiec, I.I. Kurilo, Inhibitive effect of sodium molybdate on corrosion of AZ31 magnesium alloy in chloride solutions, Electrochim. Acta 414 (2022) 140175, https://doi.org/10.1016/j.electacta.2022.140175.
[62] M.A. Osipenko, A.A. Kasach, J. Adamiec, M. Zimowska, I.I. Kurilo, D. S. Kharytonau, Corrosion inhibition of magnesium alloy AZ31 in chloride-containing solutions by aqueous permanganate, J. Solid State Electrochem. (2023), https://doi.org/10.1007/s10008-023-05472-3.
[63] J. Dziková, S. Fintová, D. Kajánek, Z. Florková, J. Wasserbauer, P. Doležal, Characterization and corrosion properties of fluoride conversion coating prepared on AZ31 magnesium alloy, Coatings 11 (2021) 675, https://doi.org/10.3390/coatings11060675.
[64] L. Yang, Y. Huang, Z. Hou, L. Xiao, Y. Xu, X. Dong, F. Li, G. Kurz, B. Sun, Z. Li, N. Hort, Microstructure, mechanical properties and fracture behaviors of large-scale sand-cast Mg-3Y-2Gd-1Nd-0.4Zr alloy, S2213956721002139, J. Magnes. Alloys. (2021), https://doi.org/10.1016/j.jma.2021.08.010.
[65] S. Pawar, X. Zhou, G.E. Thompson, G. Scamans, Z. Fan, The role of intermetallics on the corrosion initiation of twin roll cast AZ31 Mg alloy, J. Electrochem. Soc. 162 (2015) C442–C448, https://doi.org/10.1149/2.0291509jes.
[66] J. Ryl, J. Wysocka, M. Jarzynka, A. Zielinski, J. Orlikowski, K. Darowicki, Effect of native air-formed oxidation on the corrosion behavior of AA 7075 aluminum alloys, Corros. Sci. 87 (2014) 150–155, https://doi.org/10.1016/j.corsci.2014.06.022.
[67] N. Chubar, R. Gilmour, V. Gerda, M. Mičušík, M. Omastova, K. Heister, P. Man, J. Fraissard, V. Zaitsev, Layered double hydroxides as the next generation inorganic anion exchangers: Synthetic methods versus applicability, Adv. Colloid Interface Sci. 245 (2017) 62–80, https://doi.org/10.1016/j.cis.2017.04.013.
[68] A.I. Ikeuba, B. Zhang, J. Wang, E.-H. Han, W. Ke, P.C. Okafor, SVET and SIET study of galvanic corrosion of Al/$MgZn_2$ in aqueous solutions at different pH, J. Electrochem. Soc. 165 (2018) C180–C194, https://doi.org/10.1149/2.0861803jes.
[69] Q. Liu, J. Li, Z. Zhou, J. Xie, J.Y. Lee, Hydrophilic mineral coating of membrane substrate for reducing internal concentration polarization (ICP) in forward osmosis, Sci. Rep. 6 (2016) 19593, https://doi.org/10.1038/srep19593.
[70] A.E. Coy, F. Viejo, P. Skeldon, G.E. Thompson, Susceptibility of rare-earth-magnesium alloys to micro-galvanic corrosion, Corros. Sci. 52 (2010) 3896–3906, https://doi.org/10.1016/j.corsci.2010.08.006.
[71] E. Mena-Morcillo, L. Veleva, Degradation of AZ31 and AZ91 magnesium alloys in different physiological media: Effect of surface layer stability on electrochemical behaviour, J. Magnes. Alloys. 8 (2020) 667–675, https://doi.org/10.1016/j.jma.2020.02.014.
[72] L.M. Calado, M.J. Carmezim, M.F. Montemor, Rare earth based magnesium alloys—A review on WE series, Front. Mater. 8 (2022) 804906, https://doi.org/10.3389/fmats.2021.804906.
[73] P. Nowak, M. Mosiałek, D.S. Kharitonov, J. Adamiec, A. Turowska, Effect of TIG welding and rare earth elements alloying on corrosion resistance of magnesium alloys, J. Electrochem. Soc. 167 (2020) 131504, https://doi.org/10.1149/1945-7111/abb97e.
[74] C. Wang, W. Xu, D. Höche, M.L. Zheludkevich, S.V. Lamaka, Exploring the contribution of oxygen reduction reaction to Mg corrosion by modeling assisted local analysis, J. Magnes. Alloys. 11 (2023) 100–109, https://doi.org/10.1016/j.jma.2022.09.031.
[75] J. Nachtsheim, J. Burja, S. Ma, B. Markert, Long-term in vitro corrosion of biodegradable WE43 magnesium alloy in DMEM, Metals. 12 (2022) 2062, https://doi.org/10.3390/met12122062.
[76] M.C.L. de Oliveira, R.M.P. da Silva, R.M. Souto, R.A. Antunes, Investigating local corrosion processes of magnesium alloys with scanning probe electrochemical techniques: A review, J. Magnes. Alloys. 10 (2022) 2997–3030, https://doi.org/10.1016/j.jma.2022.09.024.
[77] J. Yang, C. Blawert, S.V. Lamaka, K.A. Yasakau, L. Wang, D. Laipple, M. Schieda, S. Di, M.L. Zheludkevich, Corrosion inhibition of pure Mg containing a high level of iron impurity in pH neutral NaCl solution, Corros. Sci. 142 (2018) 222–237, https://doi.org/10.1016/j.corsci.2018.07.027.